

1 **Application of ANN and RSM techniques in optimal parameter evaluation for**
2 **turbidity removal from abattoir effluent using valorized chicken bone**
3 **coagulant**

4
5 **Abstract**

6 Chicken bone coagulant (CBC) containing high grade hydroxyapatite (HPA) has been
7 applied in the coag-flocculation of abattoir effluent. The influence of process variables
8 (pH, initial concentration, dosage, Temperature, and settling time) on the effluent final
9 turbidity was investigated. Also, the accuracies of two modelling techniques (Response
10 surface methodology, RSM and Artificial neural network, ANN) in predicting the
11 non-linear nature of the system were compared. The optimization result indicates a final
12 turbidity of 4.96 mg/L (corresponding to 98.28 % removal efficiency) at pH = 6.7, dosage
13 = 1.003 g/L, initial conc. = 182.2 mg/L, coagulation temp. = 345 K and settling time of 36
14 min. Meanwhile, effluent pH was spotted as the most significant variable, with p-value
15 <0.01%. Furthermore, the error analysis result portrayed the supremacy of ANN over
16 RSM in data prediction accuracy as it signified lower error values (Mean square error,
17 MSE = 13.11 and Absolute average relative deviation, AARD = 1.43%) when compared
18 to those of RSM (MSE = 37.78, AARD = 5.93%). Thus, it was demonstrated that ANN is
19 a better tool for optimization study of the present system.

20
21 **Keywords: Abattoir-effluent, Turbidity, Hydroxyapatite, Chicken Bone, Artificial Neural**
22 **Network**

23 **1. Introduction**

24 One of the most essential ingredients for human existence and the sustaining of life as a whole
25 is fresh water. Even though there is an increased need for fresh water due to population
26 expansion and increasing urbanization (Emembolu et al., 2017). The greatest problem for those
27 who use fresh water resources is still pollution, which also jeopardizes the survival of natural
28 habitats. The release of dangerous pollutants into already stressed fresh water bodies, so
29 contaminating them, exacerbates the difficulty of assuring the supply of fresh water for the
30 teeming populace.

31 The operations of the slaughterhouse sector continue to be a significant cause of environmental
32 contamination while also serving as a key way of supplying Nigeria's enormous population with
33 protein. Approximately 6% of the nation's total GDP and 20% of the agricultural GDP are
34 contributed by the sector (Mshelbwala, 2013; Ogbeide, 2015; Ohale et al., 2022a). Animals are
35 slaughtered, washed, butchered, and then packaged in raw form for further treatment or
36 consumption as part of the fundamental meat production procedures carried out in an abattoir.
37 These operations produce a significant amount of wastewater, often known as abattoir-effluent

38 Various organic contaminants from the paunch, excrement, fat and lard, grease, unprocessed
39 food, blood, dispersed matter, urine, soluble proteins, manure, grit, condemned meat, and
40 colloidal particles are frequently present in slaughterhouse wastewater. Abattoir wastewater is
41 characterized by its foul odor, black color, and low bacteriological quality, all of which are
42 caused by these pollutants (Obi et al., 2022; Ohale et al., 2022a). The deterioration of the
43 groundwater and contamination of waterways and irrigation water with excessive organic
44 matter are both considerably exacerbated by the discharge of slaughter house wastewater into
45 the environment without proper treatment (Obi et al., 2022; Nwabanne et al., 2022).

46 In experimental and pilot size investigations, several studies have satisfactorily used a variety of
47 methodologies for the remediation of slaughterhouse wastewater. Some of the investigated
48 treatment procedures include electro-coagulation, electro-sequencing, ventilated lagoon
49 systems, high rate algal reservoirs, halophyte therapy, and integrated bio treatment systems
50 (Kundu *et al.*, 2013; Bazrafshan *et al.*, 2022; Obi et al., 2022; Ohale et al., 2022a). Some of the
51 investigated treatment procedures include electro-coagulation, electro-sequencing, ventilated
52 lagoon systems, high rate algal reservoirs, halophyte therapy, and integrated bio treatment
53 systems. The significant energy requirement for ventilation, creation of surplus sludge,
54 time-consuming processing rate brought on by buildup of suspended solids, and floating fats in
55 the reactor, unfortunately, limit the effectiveness of anaerobic treatment options (Menkiti *et al.*,
56 2015; Okan et al., 2022). Many studies still choose to use coagulation and flocculation to
57 control highly turbid pollutants due to the constraints of anaerobic treatment methods (Menkiti
58 *et al.*, 2015; Ohale et al., 2020). This can be as a result of their operational cost efficiency and
59 flexibility. In order for the large floccus to settle and be separated by decantation, the
60 coagulation and flocculation process must generate large floccus which are heavier than the
61 carrier wastewater. Three distinct and consecutive processes make up the complete coagulation
62 process: coagulant production, particle instability, and inter-particle interactions (Menkiti et al.,
63 2016; Ohale et al., 2020; Obi et al., 2022). Coagulant dose, coagulation temperature, effluent pH,
64 and effluent concentration are the key coagulation process variables. Al-Mutairi et al (2004),
65 and Amuda & Alade (2006) examined the use of poly-aluminum chloride and aluminum salt as
66 effective coagulants for the treatment of abattoir wastewater. Aquilar, *et al.*, (2005), reported
67 that treating abattoir wastewater with alum alone has a highest turbidity reduction effectiveness
68 of 87%. Furthermore, Amudaa & Alade, (2006) achieved a substantial reduction in COD from
69 abattoir effluent using 1000 mg/L of alum. Mahtaba, *et al.*, (2009) reported 99 % removal of
70 suspended solids by using 400 mg/L of alum and 30 mg/L of polymer. However, it has been

71 noted that using these synthetic coagulants have adverse health consequences. According to
72 Katayon et al. (2006), several negative effects linked with the application of chemical
73 coagulants include Alzheimer's disease, excess sludge production, cost inefficiency, and the
74 introduction of significant changes in chemical characteristics of water resulting from reactions
75 with the OH⁻ and basicity of water. Therefore, using bio-coagulants will potentially greatly
76 reduce the regular issues associated with the usage of metal salts and synthetic coagulants
77 (Katayon, *et al.*, 2006).

78 Several scientists have developed a range of organic coagulants for the treatment of severely
79 turbid waste water. Some of which are crab-shell chitin (Saritha, et al., 2015), snail shell extract
80 (Menkiti & Ejimofor, 2016), Dromedary bone (Ghedjemis et al., 2022), Periwinkle shell
81 (Menkiti, *et al.*, 2016). Recently, scientists' attention has been devoted to the use of animal bones
82 for the treatment of different forms of wastewater (Choumane et al., 2017; Brazdis et al., 2021).
83 Studies have shown that animal bones contain an active ingredient called hydroxyapatite (HAP),
84 which has been proven to be very useful in surface driven wastewater treatment processes such as
85 coagulation (Ghedjemis et al., 2022; Brazdis et al., 2021). Hydroxyapatite (HAP) has a highly
86 stable calcium phosphate hexagonal structure which can withstand extreme conditions of
87 temperature and pH. Many researchers have successfully used HAP in removal of heavy metals
88 (Marrane et a., 2022; Brazdis et al., 2021), turbidity (Choumane et a., 2017), and dye wastewater
89 (Ghedjemis et al., 2022). Therefore, our present study is essential in order to further give a
90 remedy to the environmental degradation caused by the potential for inappropriate release of
91 slaughterhouse effluents. The study examines the production of chicken bone (CB) coagulant and
92 its possible application in the coag-flocculation treatment of abattoir-effluent. Although the
93 effectiveness of numerous natural coagulants in the treatment of abattoir effluent via
94 coag-flocculation process have been widely reported in literature, however, to the best of our
95 knowledge, there has not been any reported use of chicken bone coagulant (CBC) in the treatment
96 of abattoir-effluent.

97 Previously, “one-factor at a time” (OFAT) was the strategy that most researchers used to
98 determine the best experimental parameters. However, the OFAT method is typically time- and
99 labor-intensive. Also, It rarely provides the desirable optimum that is sought after. Utilizing
100 empirical design methodological approaches, these limitations related to the usage of the OFAT
101 technique can be overcome. RSM and ANN have lately been combined as an empirical design
102 optimization algorithm in wastewater treatment research (Onu et al., 2022a; Ohale et al., 2017;
103 Nwadike et al., 2020; Onu et al., 2022b; Nwobasi et al., 2022). RSM is employed in industrial

104 processes to either produce high-quality items or run a process more efficiently (Onu et al.,
105 2021; Onu and Nwabanne, 2014). RSM's primary goal is to use experimental methods to
106 optimize an uncertain and noisy parameter using simpler approximate functions that are viable
107 over a constrained region. Numerous studies have reported using the RSM method to
108 successfully optimize process variables (Onu et al., 2020; Emembolu et al., 2022). Additionally,
109 as a result of the transdisciplinary expansion of modern analytical approaches, artificial neural
110 networks (ANNs), which are common artificial intelligence (AI) algorithms, have emerged as a
111 contemplated method for modeling resilient and non-linear systems (Ohale et al., 2022a). The
112 capability of ANN to learn from previous events and its general structure are its key
113 characteristics. It is often believed that ANN could require much more number of experiments
114 than RSM to build an efficient model. However, research has shown that a comparatively
115 smaller amount of data can still be utilized if it is statistically properly distributed throughout
116 the input vector (Shafi et al., 2018; Onu et al., 2022). Also, the experimental data of any
117 well-defined RSM would be sufficient to build an effective ANN model. Literature studies have
118 shown that ANN model consistently worked better than RSM model in predicting the response
119 of non-linear systems (Pakravan et al., 2015; Sodeifian et al., 2016).

120 This study therefore intends to critically analyze and derive a model for final turbidity reduction
121 of abattoir-effluent using the most significant process factors. The accuracy of ANN and RSM
122 techniques in modelling the coag-flocculation process will be comparatively assessed. Also, the
123 formulated objective function would be optimized using hybrid ANN-Genetic algorithm
124 (ANN-GA) technique.

125 **2 Materials and Methods**

126 **2.1. Materials**

127 The abattoir effluent was collected from a local slaughterhouse located at Amasea in Anambra
128 state, Nigeria. Chicken bones were collected from refuse were collected from fast food waste
129 around Awka, in Anambra state, Nigeria. Furthermore, analytical grade chemical reagents
130 utilized in the experiment were obtained from the Chemical Engineering Laboratory of Nnamdi
131 Azikiwe University, Awka, Nigeria.

132 **2.2. Sample pre-treatment and storage**

133 The collected abattoir-effluent was preserved by refrigeration. Prior to each stage of treatment,
134 the effluent was allowed to sediment for 24 h and afterwards decanted. Sediments which are
135 majorly composed of very fine particles which could not undergo gravity settling were
136 afterwards stored (in refrigerator) for coag-flocculation treatment. The chicken bones (CB)

137 were washed with deionized water to remove the marrow and inherent dirt, afterwards they
138 were cut into fragments of 2–5 g mass, boiled in distilled water and dried at a temperature of 90
139 °C for 8 h onto constant weight.

140 **2.3. Extraction of active coagulant**

141 The procedure reported by Brezinska-Miecznik et al., (2015) was adopted in the extraction of
142 hydroxyapatite (HPA) from chicken bones (CB). Briefly, the dried CB fragments were treated
143 with 4M NaOH solution at 90 °C for 12 days. The sample to solution ratio of the treatment was
144 kept 1 g of sample to 90 cm³ of solution. At the end of the treatment procedure, the treated
145 samples were repeatedly washed with distilled water until the pH of the filtrate approached
146 neutrality. The washed samples were dried at 150 °C for 10 h, after which they were crushed
147 using mechanized crusher to particle size of 70 µm (using a Particle Size Distribution Analyzer
148 - Model 117.08, MALVERN Instruments, USA) and then stored in an air tight container.

149 **2.4. Abattoir-effluent sample calibration and characterization**

150 In order to establish a logical link between the units of turbidity (NTU) and those of
151 concentration (mg/L), serial dilution of the raw effluent was obtained. For each of the dilute
152 solutions, characteristic concentration in NTU and the corresponding amount (mg) per volume
153 of the sample were obtained using turbidity meter (Hanna Instruments, Model: LP2000) and
154 sensitive weighing balance (JA-SARIES, Model: JA203H), respectively. Results obtained from
155 the effluent calibration were supplied in section 3.1. Furthermore, American Public Health
156 Association (APHA) standard procedure as reported by Clesceri, *et al.*, (1998) was adopted for
157 the physicochemical characterization of the abattoir-effluent. Elaborate discussion of findings
158 from the physicochemical characterization of the effluent was presented in section 3.2.

159 **2.5. Coagulant characterization**

160 The physicochemical properties and degree of effectiveness of the chicken bone coagulant
161 (CBC) extraction process was ascertained by characterization. The structural vibration,
162 topographical stabilization, and the crystallinity of the CB and CBC were determined using
163 Fourier Transform Infra-red Spectroscopy (FTIR) (ThermoNicolet Nexus Model 470/670/870),
164 Scanning Electron Microscopy (SEM) (Model Zeiss Evo@MA 17 EDX/WDS microscope), and
165 X-ray Diffraction (XRD) (PHILIPS X PERT X – RAY diffraction unit with Cu Kr radiation),
166 respectively. All the instrumental analysis was carried out according to ASTM E1508 and
167 ASTM E168 standards.

168 **2.6. Jar test procedure and experimental design**

169 The jar test procedure was carried out based on standard Bench scale nephelometric technique
 170 for investigation of water and waste water (AWWA, 2005 and WST, 2003), using Model
 171 LP-2000 Hanna Instruments Turbidimeter, Search tech Instruments 78 HW-1 magnetic stirrer
 172 and PHS-3C 005399 pH meter.

173 The pH of the effluent was adjusted to pH 3, 4, 6, 8 and 10 using 1 M H₂SO₄ and 1 M NaOH,
 174 after which appropriate amounts (0.7, 1.0, 1.6, 2.2, and 2.5 g/L) of CBC were added to each 500
 175 ml beaker containing different concentrations of abattoir effluent (100, 184, 350, 517, 600 mg/L)
 176 as illustrated in Table 2.

177 Central Composite Design (CCD) was applied in this work to model the coagulation process of
 178 turbidity removal from abattoir effluent. The design consists of a 2ⁿ factorial or fraction (coded
 179 to the usual ±1 notation) augmented by 2ⁿ axial points (±α, 0, 0,..., 0), (0, ±α, 0,..., 0),..., (0,
 180 0,..., ±α), and n_c centre points (0, 0, 0,..., 0). The statistical relevance of each parameter was
 181 evaluated using analysis of variance (ANOVA) (Ohale, *et al.*, 2017). If all variables are
 182 assumed to be measurable, the response surface can be expressed as Eq. (1). RSM optimizes the
 183 response variable (y) and searches for a suitable approximation of the functional relationship
 184 between the independent variables and the response surface.

185
$$y = b_0 + \sum b_i X_i + \sum b_{ii} X_{ii}^2 + \sum b_{ij} X_i X_j + \varepsilon \quad (1)$$

186 For statistical analysis, the experimental variable X_i has been coded as x_i as shown in Eq. 2:

187
$$x_i = \frac{X_i - X_n}{\Delta X_i} \quad (2)$$

188 Where x_i is the coded value (dimensionless) of the *i*th independent variable, X_i is the un-coded
 189 value of the *i*th independent variable, X_n is the real value of an independent variable at the
 190 centre point and ΔX_i is the step change value of the real variable *i*. The relationship between the
 191 coded value and level of variance is presented in Table 1.

192 **Table 1:** Relationship between coded value and the level of variance

Coded value	Level of variance
-α	X _{min}
-1	[(X _{min} + X _{max})/2] - [(X _{max} - X _{min}) / 2b]
0	[(X _{min} + X _{max})/2]
+1	[(X _{min} + X _{max})/2] + [(X _{max} - X _{min}) / 2b]
+α	X _{max}

193 Where; X_{\min} and X_{\max} are minimum and maximum values of X, respectively. Applying the
 194 relationships in Table 1, the values of the codes were calculated and shown in Table 2.

195 **Table 2:** Levels of independent variables for CCD experimental design

Independent variables	Symbol	Coded variable levels					
		$-\alpha$	-1	0	+1	$+\alpha$	
pH	x_1	3	4	6	8	9	
Dosage	g/L	x_2	0.7	1.0	1.6	2.2	2.5
Initial conc.	mg/L	x_3	100	184	350	517	600
Temperature	K	x_4	301	310	327.5	345	354
Settling time	min	x_5	6.3	15	32	50	59

196 The experimental plan was generated using the Design-Expert program 11.0 trial version
 197 (Stat-Ease Inc., Minneapolis, USA).

198 **2.7 Artificial neural network (ANN)**

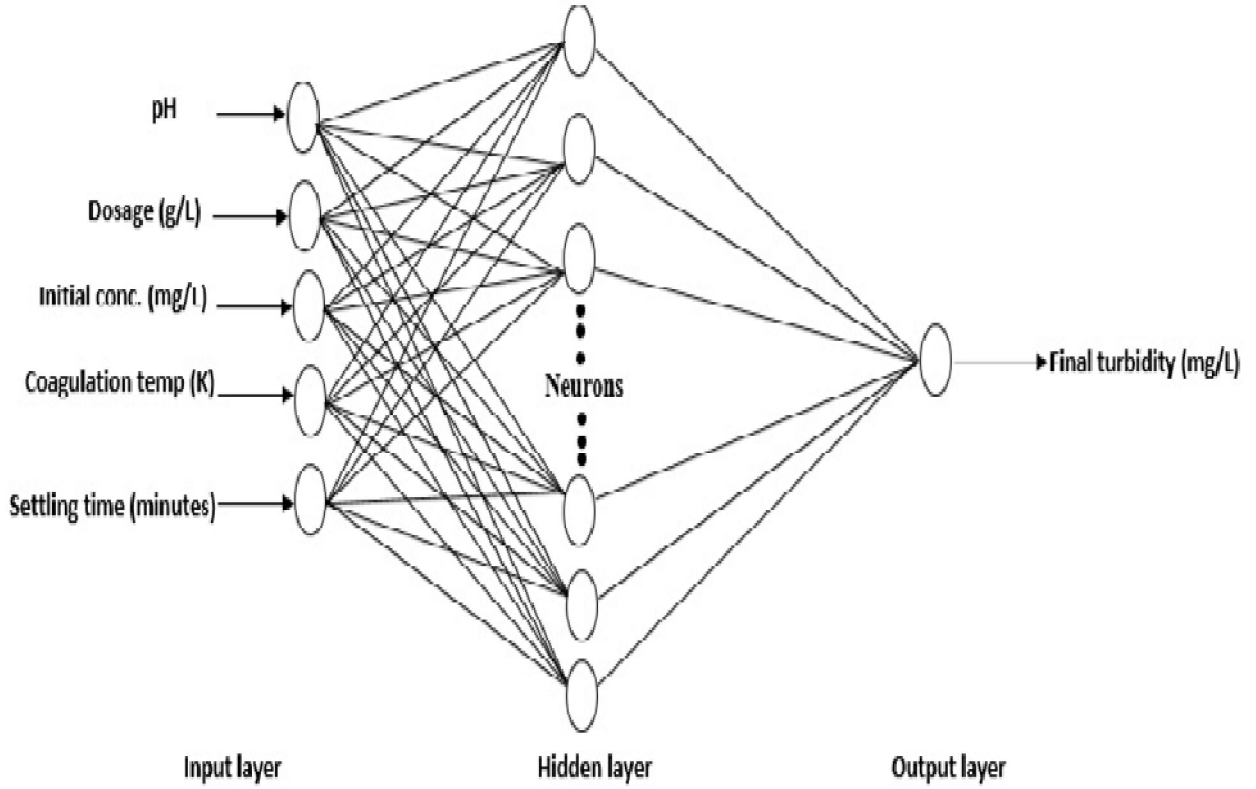
199 The creation of ANN utilized the Multi Layer Perceptron (MLP) with the Marquardt Levenberg
 200 method employing back propagation algorithm. The MLP was performed in MATLAB (The
 201 mathworks, inc., 2009 b), having five input variables comprising the input layer, and the
 202 ultimate turbidity being the sole output neuron. The biases and the total of a neuron's weighted
 203 inputs make up the input weights. The neuron is described by the mathematical statement in Eq.
 204 (3);

$$205 \quad Y_i = \sum_{i=1}^n x_i \omega_i + \theta_i \quad (3)$$

206 Where; Y_i is the net input to the node, i in the hidden layer, $w_i (i = 1, n)$ are the connection
 207 weights, θ_i is the bias and x_i is the input parameter. The weighted output was passed
 208 through a nonlinear activation process by applying the logistic output function given in Eq. (4);

$$209 \quad f(\text{sum}) = \frac{1}{1 + \exp(-\text{sum})} \quad (4)$$

210 The artificial neural network's structural framework utilized in this study is described in Fig. 1.
 211 Figure 1 shows that the output from the input layer formed an input for the hidden layer.
 212 Similarly, the output layer receives an input from the hidden layer.



213 **Fig. 1:** Architecture of the developed artificial neural network

214 A acceptable number was determined via predictive and error function testing, with the
 215 concealed number of neurons randomly ranging from 2 to 11 (see Eqs. 5 & 6, respectively) on
 216 the outputs obtained (by varying the number of neurons). The tests compare the deviation of
 217 their predictions from the experimental values (Ohale et al., 2022b).

$$218 \quad R^2 = 1 - \frac{\sum_{i=1}^{i=n} (y_{i,predic} - y_{i,exp})^2}{\sum_{i=1}^{i=n} (y_{i,exp} - y_{av})^2} \quad (5)$$

$$219 \quad RMSE = \sqrt{\frac{\sum_{i=1}^n (y_{i,predic} - y_{i,exp})^2}{n}} \quad (6)$$

220 Where n is the number of data points, $y_{i,predic}$ is the network prediction at a specific number of
 221 hidden neurons, $y_{i,exp}$ is the real experimental response, y_{av} is mean value of experimental data
 222 and i is the data index.

223
224
225

226 3. Result and discussions

227 3.1 Calibration of Abattoir effluent

228 The result of effluent calibration was presented in Fig. 2. Figure 2 shows the existence of a
229 direct proportional relationship between the amount of particles (mg) and the turbidity (NTU).
230 Linear correlation models given in Eqs. (7) and (8) were obtained from the calibration analysis
231 and were subsequently utilized in converting the concentration of abattoir effluent from NTU to
232 mg/L.

$$233 \quad C_{mg/L} = 1.841C_{NTU} - 11.368 \quad (7)$$

$$234 \quad C_{mg/L} = 1.81C_{NTU} \quad (8)$$

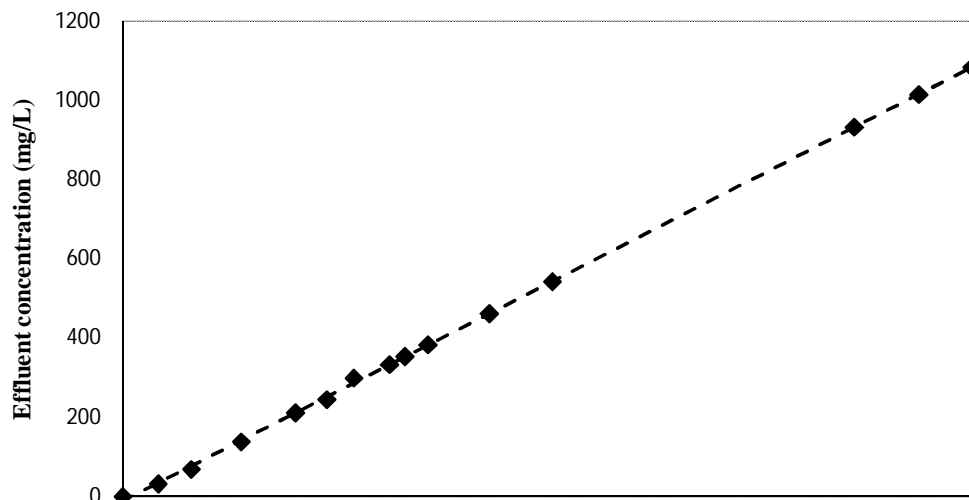
235 Where; $C_{mg/L}$ and C_{NTU} are the effluent concentrations in mg/L and NTU, respectively. Eq. (8)
236 strictly applies to abattoir effluent with very low concentrations ($NTU < 6.18$), while Eq. (7)
237 applies to abattoir effluents with turbidity concentration higher than 6.18.

238

239

240

241



248
249
250
251
252
253

254 **Fig. 2:** Abattoir-effluent calibration plot

255 **3.2. Waste water characteristics**

256 The physicochemical characteristics of the raw effluent prior to treatment is presented in Table
257 3. A close observation of Table 3 shows that only the effluent pH is within the permissible
258 discharge limit as stipulated by the Environmental Protection Act (EPA). The total suspended
259 solids (TSS) and the total solids (TS) which bear major influence on the effluent turbidity, were
260 significantly higher than the tolerable EPA threshold for effluent discharge; thus justifying the
261 need for treatment.

262 **Table 3:** Physicochemical characteristics of abattoir-effluent

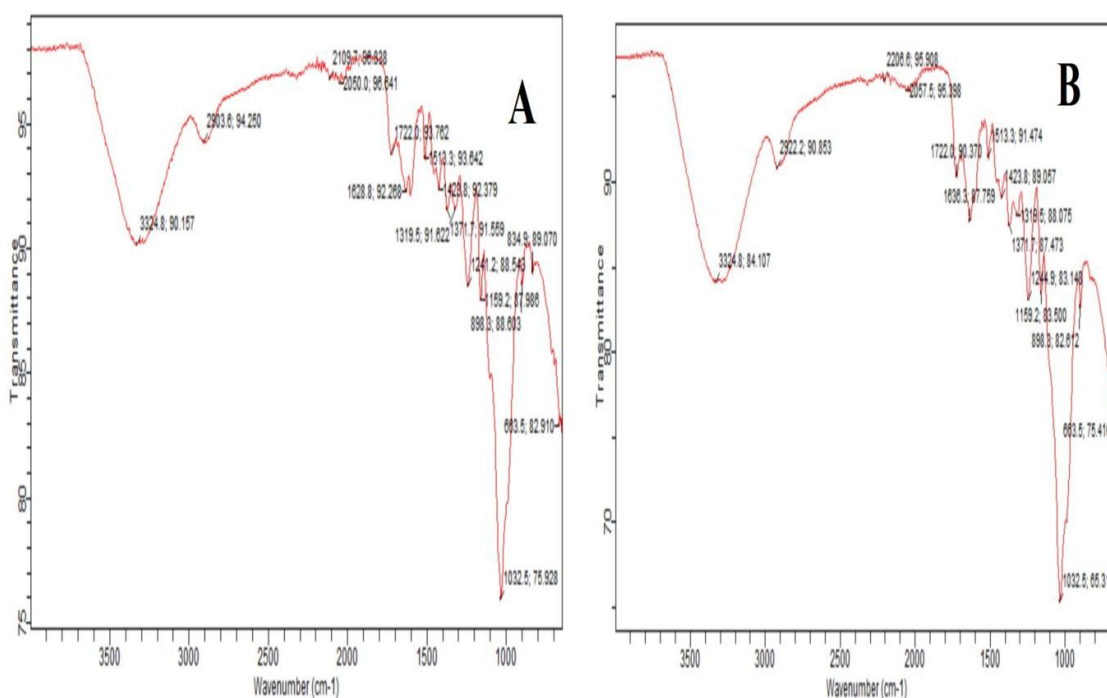
Parameters	Concentration	FEPA
Initial turbidity concentration (mg/L)	599	<100
Total suspended solids (mg/L)	1030.8	<100
Total solids (mg/L)	1614.8	<500
Biological oxygen demand (mg/L) ₅	220	210
Chemical oxygen demand (mg/L)	692	<180
pH	7.5	6 – 9
Odour	Objectionable	Odorless
Colour	Dark red	-

263
264
265

3.3 Instrumental characterization of the CSC

3.3.1 FTIR spectra analyses

266 The FTIR spectra of CB and CBC are shown in Figs. 3 (a) and 4 (b), respectively. Visual
 267 inspection of the spectra results show that the obtained CBC spectra fall within the frequency of
 268 3325 – 650 cm^{-1} . According to Coutts (2008), the observation peaks below 600 cm^{-1} are not
 269 applicable for characterizing wavebands. The vibrational peak at 663.5 cm^{-1} which is attributed
 270 to OH functional group, became more conspicuous in CBC following NaOH treatment. The
 271 absorption intensity at 1241.2 cm^{-1} in the raw CB shifted to 1244.9 cm^{-1} after the HAP
 272 extraction process. This waveband (1241.2 cm^{-1}) demonstrates the presence of CO_3^{2-} which
 273 indicates a major characteristic property of HAP. The peak at 1032.5 cm^{-1} indicates the
 274 presence of C–O bending of the glucose molecule due to C–O–C linkage. The presence of
 275 phosphorus compound (P–F stretching) is displayed on 898.3 cm^{-1} , while its presence in the
 276 CBC (HPA) spectra shows the presence of N – H wagging band of the protein compounds. The
 277 C–O stretching band at 1159.2 cm^{-1} indicates the presence of anhydrides in the CBC; while
 278 those at 3324.8 cm^{-1} suggest the presence of N – H amides (Brzezińska-Miecznik et al., 2014).

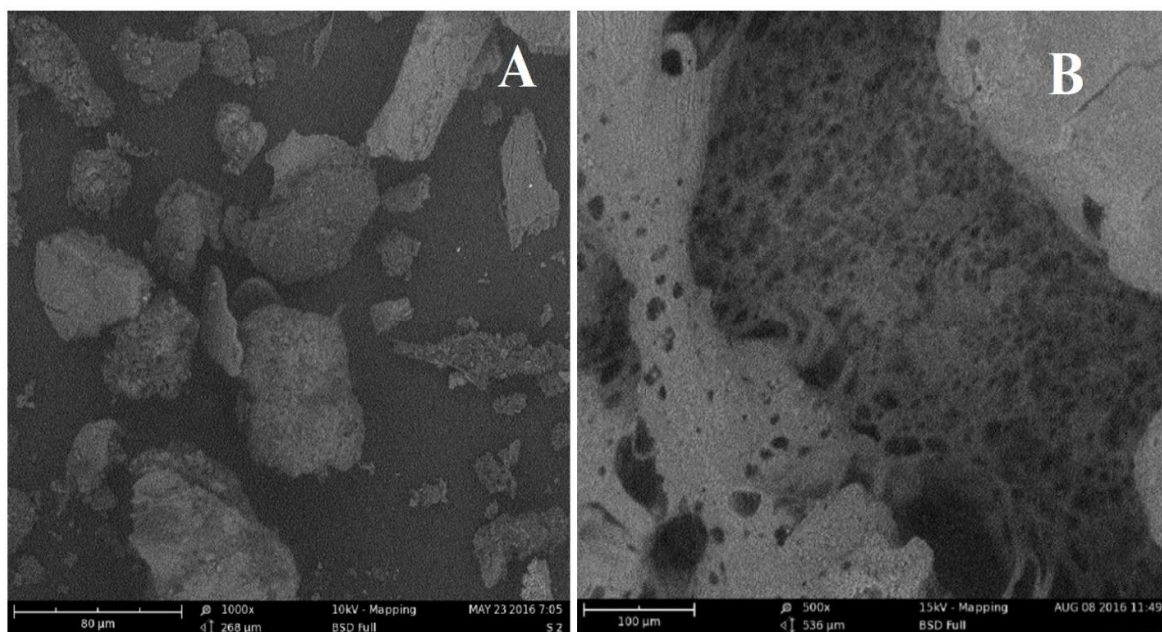


279
 280 **Fig. 3:** FTIR spectra of (a) CB (b) CBC
 281

282 3.3.2 SEM image analyses

283 Figs. 4 (a) and (b) represents the scanning electron micrograph of CB and CBC, respectively.
 284 The SEM image of CB reveals the appearance of irregular platelet. This suggests that CB
 285 possesses rough edges, with crispy properties; a unique feature of animal tissues with high

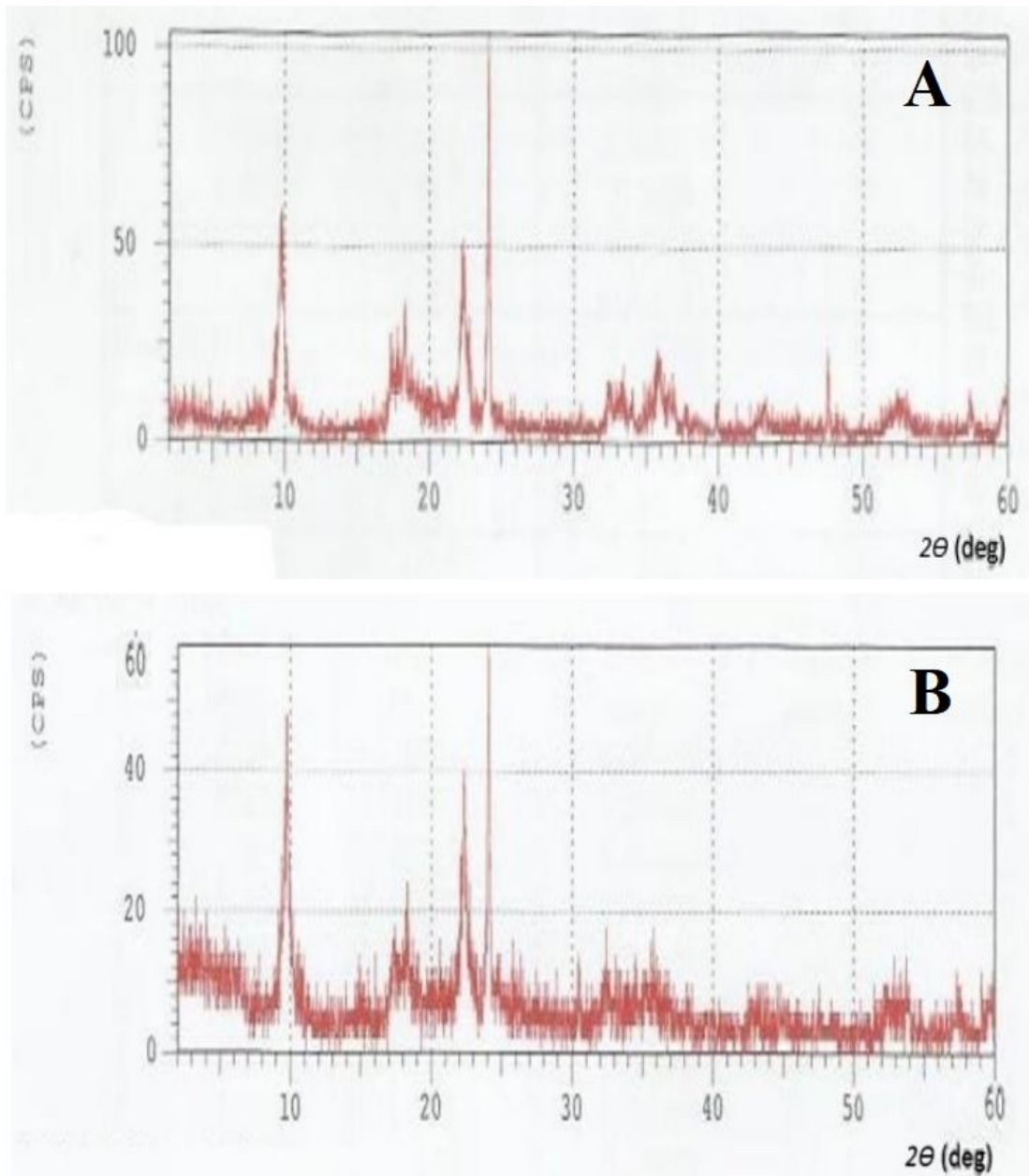
286 calcium content. Similarly, comparison of Fig 4 (b) and Fig 4 (a) shows characteristic
287 improvement in the morphological features. Some of these improvements such as the formation
288 of better cohesion, reduced individual lamella and the presence of a highly porous dark field
289 matrix could be a direct consequence of HPA extraction process. This improved porous
290 property is important for enhanced particle sticking required for surface phenomenon driven
291 matrices like coagulation.



292
293 **Fig. 4:** SEM micrograph of (a) CB (b) CBC

294 3.3.3. XRD analyses

295 The polymorphic features of a compound with different crystalline structures are determined
296 using x-ray diffraction technique. The XRD pattern of CB and CBC are depicted in Figs. 5 (a)
297 & (b), respectively. The XRD pattern of CB depicts a well organized spectral pattern with
298 strong reflections 2θ values at $8 - 10$, $17 - 19$, $23 - 35$ and $33 - 37^\circ$. While the XRD pattern of
299 CBC shows similar reflections as those of CB at 2θ values but with low intensity peaks. The
300 unorganized nature of the CBC spectral pattern and its low intensity values indicates that the
301 CBC is a less crystalline poly-morph when compared to CB.



302
 303 **Fig. 5:** XRD pattern for (a) CB (b) CBC
 304

305 **3.4. RSM modelling**

306 The combined effects of effluent pH, coagulant dosage, initial concentration, coagulation
 307 temperature and settling time on effluent turbidity reduction was studied using central
 308 composite design. The five-input experimental (consisting of 16 factorial points, 10 axial and 6
 309 centre points) as well as the predicted values of percentage turbidity removal are presented in
 310 **Table 4**. Also, **Table 5** shows the relevant parameters generated from the analysis of variance
 311 (ANOVA). It should be noted that ANOVA technique employs the p-value and F-value to

312 determine the adequacy and fitness of the empirical model. Hence, by comparing the model and
 313 lack of fit parameters, an F-value of 189.043 and a low p-value of 0.0001 as shown in **Table 5**
 314 implies that the model is significant. The model p-value of 0.0001 indicates that there is only
 315 0.01% chance that the model F-value could occur due to noise. The values of “prob > F” less
 316 than 0.0500 indicate that model terms are significant. Consequently,
 317 $x_1, x_2, x_3, x_5, x_1x_3, x_1x_4, x_1x_5, x_2x_4, x_2x_5, x_3x_4, x_3x_5, x_1^2, x_2^2$ and x_5^2 are significant
 318 model terms. The lack of fit f-value of 0.91 implies the lack of fit is not significant relative to
 319 pure error, and there is 58.59% chance that a lack of fit f-value this large could occur due to
 320 noise. This value of lack of fit implies that the model is well fitted (Ohale et al., 2022a). The
 321 smaller the magnitude of p-value, the greater the significance of the corresponding model term.
 322 From **Table 5**, effluent pH and coagulation temperature have the highest and the least influence
 323 respectively, on the final turbidity of the effluent, which is in agreement with the findings of
 324 other researchers (Menkiti et al., 2015, Ohale et al., 2020). The predicted R-squared of 0.9675
 325 is in reasonable agreement with the adjusted R-squared of 0.9765 because they are < 0.2 apart
 326 (Ohale et al., 2022a).

327 **Table 4:** The CCD matrix along with the experimental and predicted values

Std order	Point type	pH	Dosage (g)	Initial			EXP	RSM	ANN
				Conc. (mg/L)	Temp. (K)	time (min)			
1	Factorial	-1	-1	-1	-1	1	197.9	201.1	197.9
2	Factorial	1	-1	-1	-1	-1	19.3	23.6	19.3
3	Factorial	-1	1	-1	-1	-1	167.9	171.1	167.9
4	Factorial	1	1	-1	-1	1	64.1	66.4	63.3
5	Factorial	-1	-1	1	-1	-1	294.7	300.7	294.7
6	Factorial	1	-1	1	-1	1	88.8	84.0	88.8
7	Factorial	-1	1	1	-1	1	117.1	113.2	118.7
8	Factorial	1	1	1	-1	-1	101.1	108.4	101.1
9	Factorial	-1	-1	-1	1	-1	30.8	32.3	30.8
10	Factorial	1	-1	-1	1	1	82.3	81.8	81.9
11	Factorial	-1	1	-1	1	1	137.0	135.3	137.0
12	Factorial	1	1	-1	1	-1	111.5	112.2	111.5
13	Factorial	-1	-1	1	1	1	156.6	157.8	156.6
14	Factorial	1	-1	1	1	-1	61.0	54.5	61.0
15	Factorial	-1	1	1	1	-1	424.1	418.5	424.1
16	Factorial	1	1	1	1	1	100.9	103.3	101.7
17	Axial	-1.5	0	0	0	0	285.3	283.6	285.3

18	Axial	1.5	0	0	0	0	118.1	115.7	118.1
19	Axial	0	-1.5	0	0	0	122.0	120.2	122.0
20	Axial	0	1.5	0	0	0	177.2	175.0	177.2
21	Axial	0	0	-1.5	0	0	47.8	48.9	47.8
22	Axial	0	0	1.5	0	0	144.0	155.5	144.0
23	Axial	0	0	0	-1.5	0	118.6	100.2	118.6
24	Axial	0	0	0	1.5	0	106.2	105.3	106.2
25	Axial	0	0	0	0	-1.5	66.5	60.3	66.5
26	Axial	0	0	0	0	1.5	5.9	8.1	5.9
27	Center	0	0	0	0	0	102.1	102.7	102.6
28	Center	0	0	0	0	0	95.8	102.7	102.6
29	Center	0	0	0	0	0	116.8	102.7	102.6
30	Center	0	0	0	0	0	93.1	102.7	102.6
31	Center	0	0	0	0	0	104.6	102.7	102.6
32	Center	0	0	0	0	0	94.1	102.7	102.6

328

329

330 **Table 5:** Analysis of variance table

Source	Sum of squares	dF	Mean square	F – value	p-value	
Model	214254.700	15	14283.647	189.043	< 0.0001	Significant
x ₁	64261.909	1	64261.909	850.502	< 0.0001	
x ₂	6852.238	1	6852.238	90.689	< 0.0001	
x ₃	22364.783	1	22364.783	295.996	< 0.0001	
x ₄	59.070	1	59.070	0.782	0.3897	
x ₅	6205.656	1	6205.656	82.131	< 0.0001	
x ₁ x ₃	9225.041	1	9225.041	122.093	< 0.0001	
x ₁ x ₄	778.620	1	778.620	10.305	0.0055	
x ₁ x ₅	7744.497	1	7744.497	102.498	< 0.0001	
x ₂ x ₄	21981.617	1	21981.617	290.925	< 0.0001	
x ₂ x ₅	15970.407	1	15970.407	211.367	< 0.0001	
x ₃ x ₄	3257.661	1	3257.661	43.115	< 0.0001	
x ₃ x ₅	20251.712	1	20251.712	268.030	< 0.0001	
x ₁ ²	22189.884	1	22189.884	293.682	< 0.0001	
x ₂ ²	4751.627	1	4751.627	62.887	< 0.0001	
x ₅ ²	11103.631	1	11103.631	146.956	< 0.0001	
Residual	1208.922	16	75.558			
Lack of Fit	806.794	11	73.345	0.912	0.5849	not significant
Std. Dev.	8.69		R-Squared	0.9944		
Mean	123.54		Adj R-Squared	0.9891		
C.V. %	7.04		Pred R-Squared	0.9765		

331

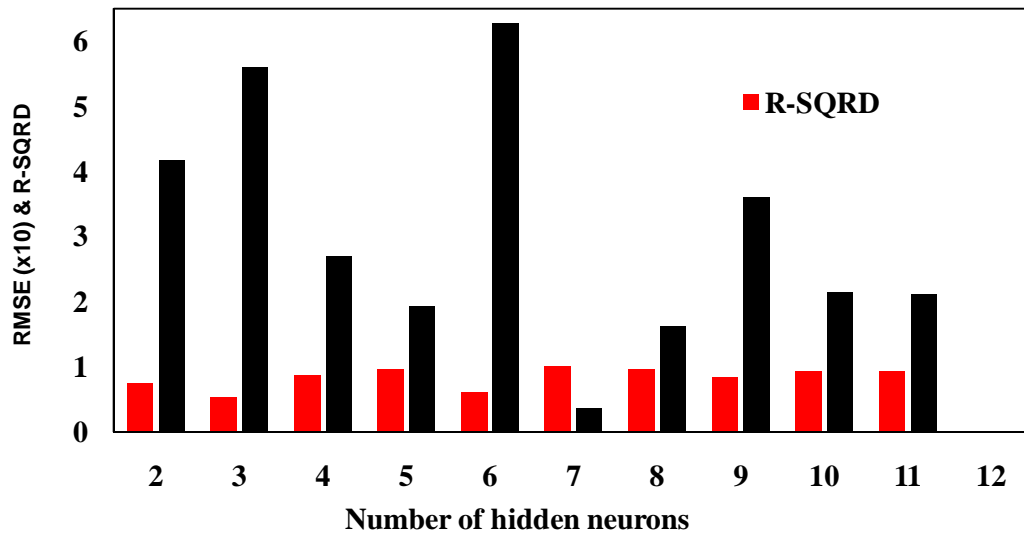
332 The final equation in terms of the coded factors is expressed as Eq. 9;

$$\begin{aligned}
 \text{Finalturbidity} = & 102.73 - 55.99x_1 + 18.28x_2 + 35.88x_3 + 1.70x_4 - 17.40x_5 - 26.68x_1^2 \\
 & + 6.9x_1x_4 + 22.0x_1x_5 + 37.07x_2x_4 - 31.59x_2x_5 + 15.85x_3x_4 - 39.53x_3x_5 \\
 & + 43.08x_1^2 + 19.94x_2^2 - 30.48x_3^2
 \end{aligned} \tag{9}$$

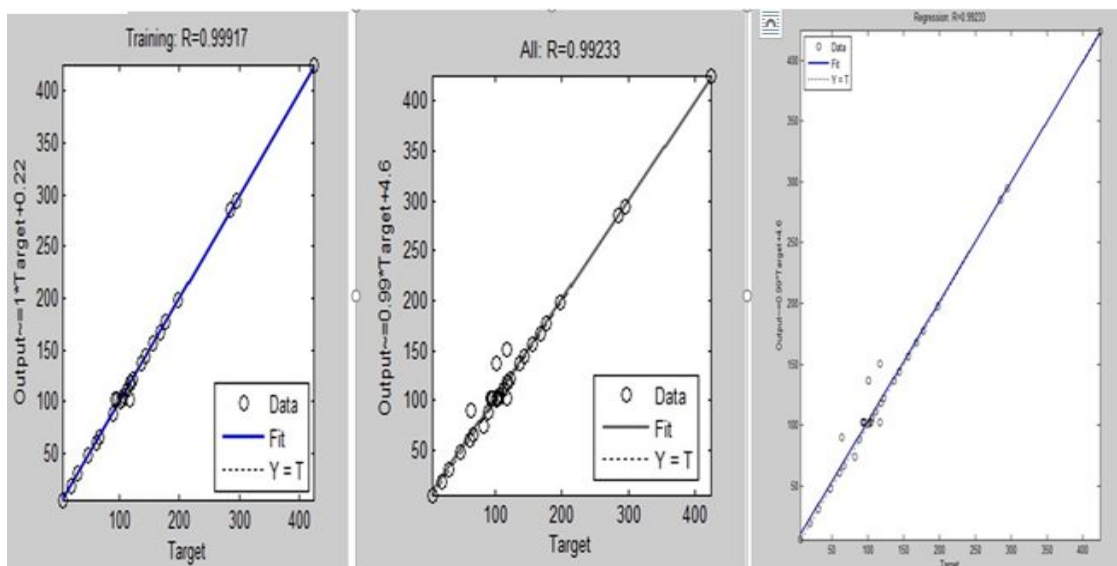
335 **3.5. ANN modelling**

336 Data set employed in ANN modeling was identical to those used in design of experiment (see
 337 Table 5). The graphical expression for the topological analysis is displayed in Fig. 6. Data
 338 partitioning as training set and test set were conducted to eliminate the issue of over-training
 339 and over parametrization. The 7 selected hidden neuron numbers produced the highest
 340 correlation coefficient (0.988) and the least root mean square error (RMSE) value (0.3701).
 341 Also, the regression plot (Fig. 7) showed a relatively high correlation coefficient ($R^2 > 0.95$);
 342 thus suggesting a good correlation between the experimental and ANN predicted values.

343



361 **Fig.6:** Effect of the neuron numbers in the hidden layer on the performance of the
 362 neural network



363 **Fig. 7.** Regression analysis for ANN predicted values versus exp. (target) values

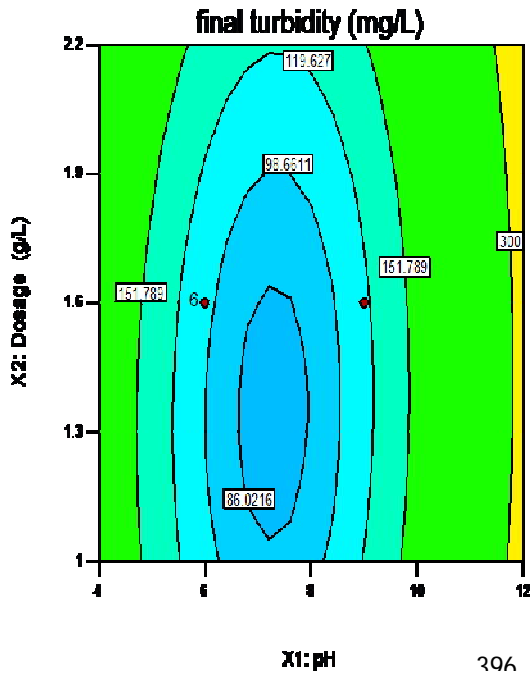
364 **3.6. Combined effect of operating parameters on final turbidity**

365 The contour plot in Figs. 8 – 11 shows the result for the combined effects of various process
 366 variables on the abattoir effluent final turbidity. The reduced effluent final turbidity (80.3 mg/L)
 367 observed in Fig. 8 was occasioned by an increased coagulant dose (from 1.0 g/L to 1.3 g/L) at a
 368 constant pH. Further increase in coagulant dosage (beyond 1.3 g/L) impacted the final effluent
 369 turbidity negatively, as the removal efficiency of suspended particles decreased significantly

370 (see Fig. 11). The observed decrease in final turbidity with increase in the coagulant dose (up to
371 1.3 g/L) could be due to the availability of more active sites necessary for coagulation process.
372 According to Menkiti and Ejimofor (2016), re-turbidization is caused by charge reversal due to
373 over concentration of positively charged coagulant particles. This explains the reduction in
374 turbidity removal efficiency (re-turbidization) when the coagulant dose is augmented beyond
375 1.3 g/L.

376 The combined effect of effluent pH and initial concentration is shown in Fig. 9. It could be
377 observed that the coagulant displayed maximum turbidity reduction (58.6 mg/L) at neutral
378 environment (pH 6.7) and at constant effluent initial concentration of 183.0 mg/L. Such
379 observation could be explained by the fact that the buffer nature of the effluent tends to enhance
380 the precipitation of the coagulant around neutral pH ($6.5 \leq pH \leq 7.0$). However, the
381 adjustment of the effluent pH either to the acidic or alkaline region was met with a significant
382 reduction in turbidity removal efficiency (*final turbidity* < 50.0 mg/L). This is due to the
383 disappearance of the effluent buffer nature at pH values outside the neutral environment; thus
384 resulting in coagulant precipitation difficulties. The effect of initial effluent concentration
385 shows that low initial concentration of raw effluent results in a low final turbidity. However, an
386 increment in the effluent initial concentration results in low removal efficiency and a high final
387 turbidity value. This phenomenon could be attributed to lack of sufficient active site for the
388 removal of turbid particles at high concentration.

389 The effect of coagulation temperature and settling time is shown in the 2-D contour plot of Fig.
390 10. It could be observed that at high temperature, an accelerated settling rate was recorded; thus
391 resulting in low final turbidity of the treated effluent. This observation could be explained by
392 the fact that temperature increase bears positive effect on coagulation and flocculation process
393 by altering the solubility and also reduces the effluent viscosity, thereby allowing for higher
394 dispersion of CBC particles which aided floc formation and cell enmeshment (Ohale et al.,
395 2020).



397 **Fig. 8.** 2D contour for the combined effects of coagulant dosage and effluent pH

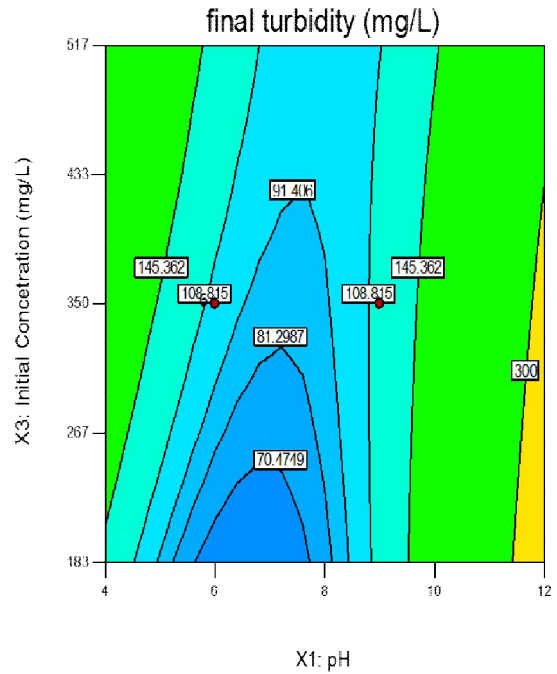
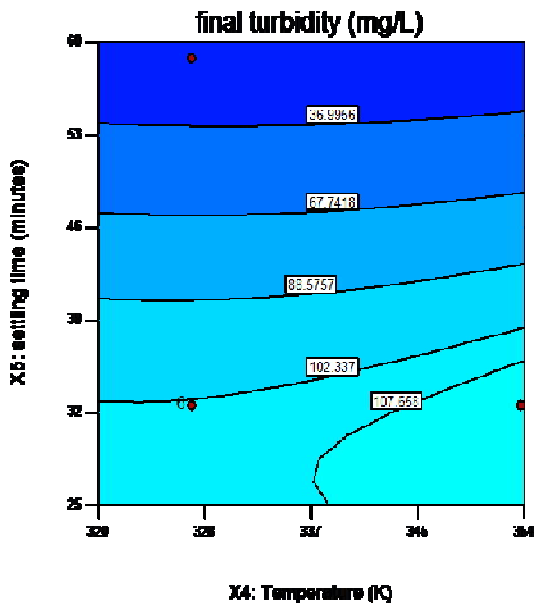


Fig. 9. 2D contour for the combined effects of effluent initial concentration and effluent pH



398 **Fig. 10.** 2D contour for the combined effects of settling time and coagulation temperature
399

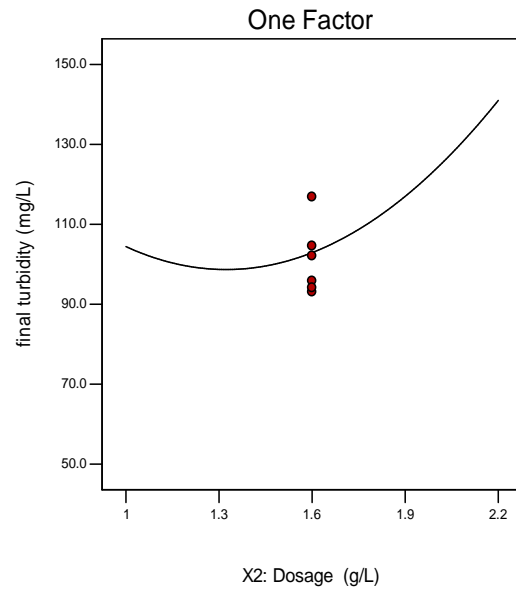


Fig. 11. Effect of coagulant dosage on the final turbidity.

400 **3.7. ANN and RSM comparative analyses**

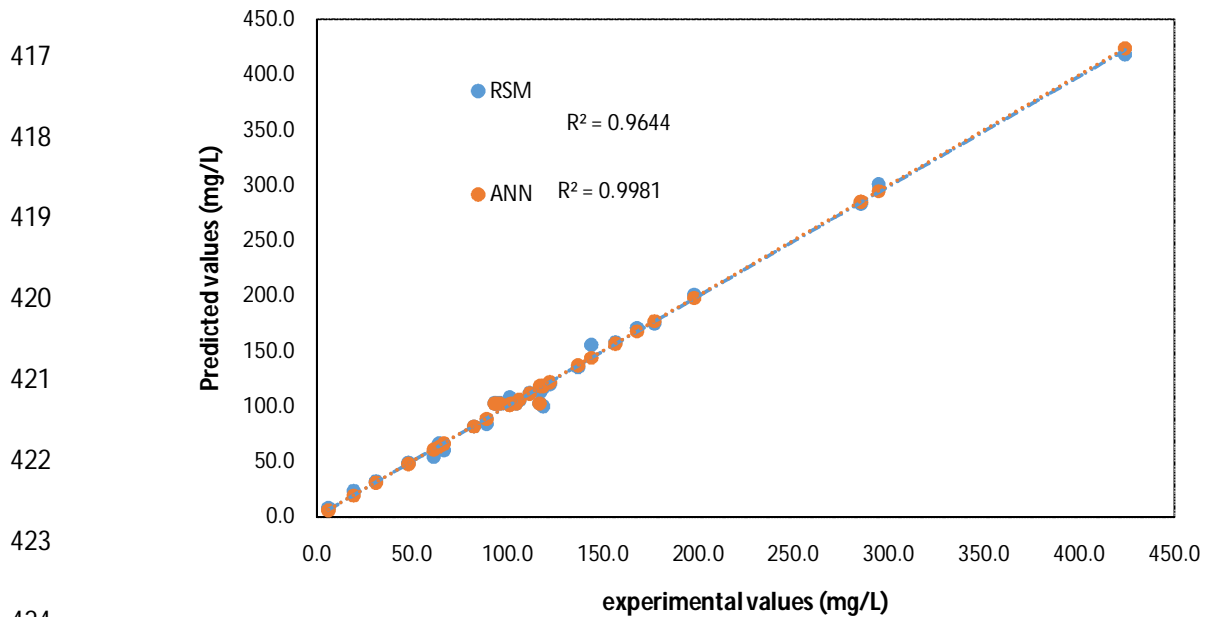
401 In order to ascertain the superiority of either of the optimization tools (ANN and RSM) over the
 402 other in predicting the non-linear behavior of the present system, error functions were
 403 employed. The coefficient of determination (R^2), mean square error (MSE), and absolute
 404 average relative deviation (AARD) were the error functions used to compare the predictions
 405 accuracy of both models. MSE and AARD values were evaluated from Eqs.10 & 11,
 406 respectively; while the coefficient of determination (R^2) values was estimated from Fig. 12.
 407 From the values of R^2 , MSE and AARD shown in **Table 6**, the ANN predictions produced a
 408 higher regression coefficient and a negligible deviation from experimental values when
 409 compared to the RSM predictions. This confirms that ANN technique as against RSM
 410 technique portrayed better accuracy in capturing the non-linear nature of the coagulation
 411 process.

$$412 \quad MSE = \frac{1}{n} \sum_{i=1}^n (y_{i, predic.} - y_{i, exp.})^2 \quad (10)$$

$$413 \quad AARD(\%) = \frac{1}{n} \sum_{i=1}^n \left(\left| \frac{(y_{i, predic.} - y_{i, exp.})}{(y_{i, exp.})} \right| \right) \times 100 \quad (11)$$

414 Where; $y_{i, predic.}$, $y_{i, exp.}$ and n are final turbidity obtained by the predicted model, the
 415 experimental data and the number of experimental data, respectively.

416



424

425

Fig. 12: RSM and ANN model appraisal

426

427

428

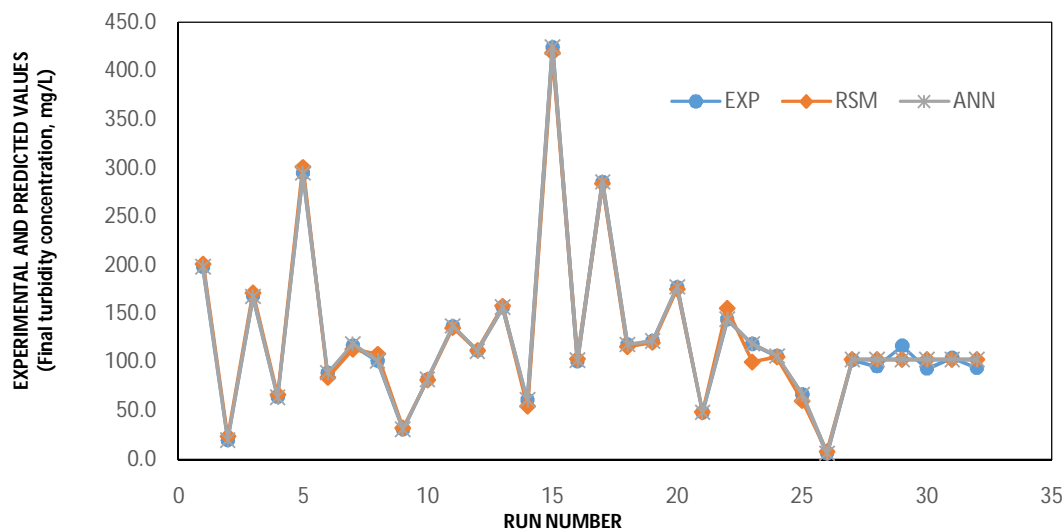
Table 6: Comparison of predictive competency of RSM and ANN

	RSM	ANN
MSE	37.78	13.11
R ²	0.9644	0.9981
AARD	5.93	1.43

429

430 Fig. 13 shows the comparative parity plot for the RSM, ANN models and the experimental data
 431 versus experimental run number. High correlation could be observed between the ANN and
 432 experimental data points. Meanwhile, in comparison with the experimental data point, the RSM
 433 data point showed significant deviations especially at run numbers 14, 22 and 23; with
 434 magnitudes of 5.6, 11.4 and 18.4, respectively. The correlation depicted by ANN data points in
 435 relation to the experimental values further gave credence to the superiority of ANN model over
 436 the RSM model with respect to the present study.

437



445 **Fig. 13:** A plot depicting the comparison between the experimental and predicted values for
 446 the ANN and RSM models

447 **3.8. Optimization using ANN-Genetic Algorithm (ANN-GA) technique**

448 The objective of process optimization is to search for the optimum process conditions to
 449 establish the minimum final turbidity. In this approach, the ANN-GA was used to generate the
 450 model values. Eqs. 12 – 16 show the selected range of constraints for each variable. Also, the
 451 technique of hybrid ANN-GA algorithm used in this work is illustrated in Fig. 14.

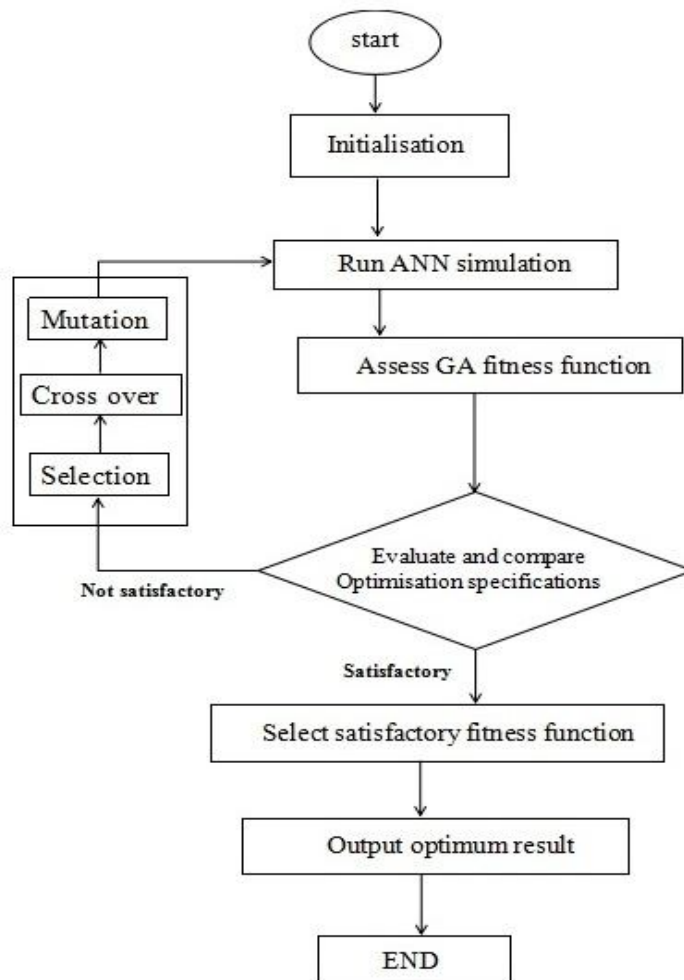
452 $6.5 \leq pH \leq 7.5$ (12)

453 $1.0 \text{ g / L} \leq dosage \leq 1.5 \text{ g / L}$ (13)

454 $183 \text{ mg / L} \leq initialcon \ c. \leq 250 \text{ mg / L}$ (14)

455 $310 \text{ K} \leq Temp . \leq 345 \text{ K}$ (15)

456 $30 \text{ min .} \leq settling \ time \leq 50 \text{ min .}$ (16)



470 **Fig. 14:** Flow chart of combining ANN-GA optimisation technique.

471

472

473

474

475 However, based on afore mention evaluation an optimal final turbidity of 4.96 mg/L was
 476 obtained pH = 6.7, dosage = 1.003 g/L, initial conc. = 182.2 mg/L, coagulation temperature =
 477 345 K and settling time = 36 min. Duplicate validation experiments were conducted in order to
 478 uphold the optimal predicted value. Using the optimum variable conditions, the average final
 479 turbidity obtained was 5.53 ± 0.24 (mg/L). The treated effluent obtained after the validation
 480 experiment was characterized and the results are shown on Table 7. The characterization result
 481 shows that the model prediction was in agreement with the experimental value.

482 **Table 7:** Post optimal characterization results of the abattoir waste water

Parameter	Treated abattoir
Final turbidity concentration (mg/L)	5.3
Total suspended solids (mg/L)	2.5
Total solids (mg/L)	3.1
Biological oxygen demand (mg/L)	8.6
Chemical oxygen demand (mg/L)	152
pH	8.1
Odour	Slightly alkaline
Colour	Clear colourless

483

484 4. Conclusion

485 In this work, the coag-flocculation of abattoir waste water was studied using HPA derived from
 486 raw CB. RSM and ANN modelling techniques were comparatively used in predicting the final
 487 turbidity of the effluent. Statistical techniques (R^2 and RMSE) were employed in selecting the
 488 most appropriate hidden number of neurons. Multi-layer neural network (5-7-1) was chosen to
 489 develop accurate and complex nonlinear relationship. From the results of the comparative
 490 analysis, ANN model was found to perform better in capturing the non-linear nature of the
 491 system. Process optimization using ANN-GA technique gave an optimum value of 4.92 mg/L
 492 for final effluent turbidity at pH = 6.7, dosage = 1.003 g/L, initial conc. = 182.2 mg/L,
 493 coagulation temperature = 345K and settling time = 36 min. This value was validated by a set
 494 of duplicate experiments producing an average value of 5.53 ± 0.24 (mg/L) which is in close
 495 agreement with the predicted value.

496

497 Funding

498 This research work was supported by the Tertiary Education Trust Fund, Nigeria through
499 Institution Based Research grant (IBR). Years: TETFUND Research Projects (RP) Intervention
500 Funds, (2017).

501 **References**

502

503 Mshelbwala GM, (2013). National Livestock Policy Focal Point Presentation – Nigeria.
504 Paper presented at Side-meeting of NLPFPS on VET-GOV programme engagement /
505 targetting and capacity building facilitation Abidjan, Cote D'ivoire.

506 Ogbuide, O. A., 2015. Meat Industry Development in Nigeria: Implications of the Consumers'
507 Perspective. Mayfair Journal of Agribusiness Management. 1, 59 - 75.

508 Ohale, P.E., Onu, C. E., Nwabanne, J. T., Aniagor, C. O., Okey-Onyesolu, C. F., Ohale, N. J.,
509 2022. A comparative optimization and modeling of ammonia–nitrogen adsorption from
510 abattoir wastewater using a novel iron-functionalized crab shell. Applied Water Science
511 12:193: 1 – 27. <https://doi.org/10.1007/s13201-022-01713-4>

512 Obi, C. C., Nwabanne, J. T., Igwegbe, C. A., Ohale, P. E., Okpala, C. O. (2022).
513 Multi-characteristic optimization and modeling analysis of electrocoagulation
514 treatment of abattoir wastewater using iron electrode pairs. Journal of Water Process
515 Engineering, 49, 103136. <https://doi.org/10.1016/j.jwpe.2022.103136>

516 Kundu, P., Debsarkar, A., Mukherjee, S., 2013. Treatment of Slaughter House Wastewater
517 in a Sequencing Batch Reactor: Performance Evaluation and Biodegradation Kinetics.
518 Hindawi Publishing Corporation BioMed Research International. 11, 1 - 15.
519 <https://doi.org/10.1155/2013/134872>

520 Bazrafshan, E., Zakeri, H.R., Vieira, M.G.A., Derakhshan, Z., Mohammadi, L.,
521 Mohammadpour, A., Mousavi Khaneghah, A., (2022). Slaughterhouse Wastewater
522 Treatment by Integrated Chemical Coagulation and Electro-Fenton Processes, Sustainability
523 14, 11407. <https://doi.org/10.3390/su141811407>

524 Menkiti, M. C., Sekaran, G., Ugonabo, V. I., Menkiti, U. N., Onukwuli, O. D., (2015).
525 Factorial Optimisation and Kinetic studies of coagulation-flocculation of brewery effluent
526 by crab shell coagulant. Journal of Chinese Advanced Materials Society, 4, 36 – 61.
527 <https://doi.org/10.1080/22243682.2015.1048287>

528 Ohale, P. E., Onu, C. E., Ohale, N. J., Oba, S. N., (2020). Adsorptive kinetics, isotherm and
529 thermodynamic analysis of fishpond effluent coagulation using chitin derived coagulant
530 from waste Brachyura shell, Chemical Engineering Journal Advances, 4, 100036.
531 <https://doi.org/10.1016/j.ceja.2020.100036>

532 Menkiti, M. C., Ejimofor, M., (2016). Experimental and artificial neural network application
533 on the optimization of paint effluent (PE) coagulation using novel acatinodea shell extract
534 (ASE). JWPE. 10, 172-187. <https://doi.org/10.1016/j.jwpe.2015.09.010>

535 Al-Mutairi, N. Z., Hamoda, M. F., Al-Ghusain, I., (2004). Coagulant selection and sludge
536 conditioning in a slaughterhouse wastewater treatment plant. Bioresource Technology. 95,
537 115 – 119. <https://doi.org/10.1016/j.biortech.2004.02.017>

- 538 Amuda, O. S., Alade, A., (2006). Coagulation/flocculation process in the treatment of abattoir
539 wastewater. *Desalination* 196, 22–31. <https://doi.org/10.1016/j.desal.2005.10.039>
- 540 Aquilar, M. I., Sáez, J., Llorens, S. M., Ortuño, J. F., Meseguer, V., Fuentes, A., (2005).
541 Improvement of coagulation-flocculation process using anionic polyacrylamide as coagulant
542 aid. *Chemosphere*.58,47 – 56. <https://doi.org/10.1016/j.chemosphere.2004.09.008>
- 543 Mahtaba, A., Tariq, M., Shafiq, T., Nasir, A., (2009). Coagulation/adsorption combined
544 treatment of slaughterhouse wastewater. *Desalination and Water Treatment* 12,
545 270–275. <https://doi.org/10.5004/dwt.2009.952>
- 546 Katayon, S., Megat-Mohd, M. J., Asma, M., Abdul-Ghani, L. A., Thamer, A. M., Azni, I.,
547 Ahmad, J., Khor, B. C., Suleyman, A. M., (2006). Effects of storage conditions of Moringa
548 Oleifera seeds on its performance in coagulation. *Bioresource Technology* 97, 1455–60.
549 <https://doi.org/10.1016/j.biortech.2005.07.031>
- 550 Ghedjemis, A., Riad Ayeche, R., Maya Kebaili, M., Ali Benouadah, A., Laurent Frédéric
551 Gil, L. (2022). Application of natural hydroxyapatite in the treatment of polluted water:
552 Utilization of dromedary bone as bioadsorbent, *International of applied ceramic technology*.
553 <https://doi.org/10.1111/ijac.14041>
- 554 Choumane, F. Z., Benguella, B., Maachou, B., Saadi, N. (2017). Valorisation of a
555 bioflocculant and hydroxyapatites as coagulation-flocculation adjuvants in wastewater
556 treatment of the steppe in the wilaya of Saida (Algeria), *Ecological Engineering* 107,
557 152–159. <http://dx.doi.org/10.1016/j.ecoleng.2017.07.013>
- 558 Brazdis, R.I., Fierascu, I., Avramescu, S.M., Fierascu, R.C. (2021). Recent Progress in the
559 Application of Hydroxyapatite for the Adsorption of Heavy Metals from Water Matrices.
560 *Materials*, 14, 6898. <https://doi.org/10.3390/ma14226898>
- 561 Marrane, S. E., Dänoun, K., Allouss, D., Sair, S., Channab, B., Rhihil, A., Zahouily, M.
562 (2022). A Novel Approach to Prepare Cellulose□g□Hydroxyapatite Originated from Natural
563 Sources as an Efficient Adsorbent for Heavy Metals: Batch Adsorption Optimization via
564 Response Surface Methodology. *ACS Omega*, 7, 28076–28092.
565 <https://doi.org/10.1021/acsomega.2c02108>
- 566 Onu, C. E., Igbokwe, P. K., Nwabanne, J. T., & Ohale, P. E. (2022a). ANFIS, ANN, and
567 RSM modeling of moisture content reduction of cocoyam slices. *Journal of Food Processing*
568 *and Preservation* 46, 10 <https://doi.org/10.1111/jfpp.16032>
- 569 Ohale, P. E., Uzoh, C. F., Onukwuli, O. D. (2017). Optimal factor evaluation for the dissolution
570 of alumina from Azaraegbelu clay in acid solution using RSM and ANN comparative
571 analysis, *South African Journal of Chemical Engineering* 24, 43 – 54.
572 <https://doi.org/10.1016/j.sajce.2017.06.003>
- 573 Nwadike, E. C., Abonyi, M. N., Nwabanne, J. T., Ohale, P. E. (2020). Optimization of Solar
574 Drying of Blanched and Unblanched Aerial Yam using Response Surface Methodology,
575 *International Journal of Trend in Scientific Research and Development*, 4 (3), 659 – 666.

- 576 Onu et al., (2022b). Modeling, optimization, and adsorptive studies of bromocresol green
577 dye removal using acid functionalized corn cob, *Cleaner Chemical Engineering* 4, 100067.
578 <https://doi.org/10.1016/j.clce.2022.100067>
- 579 Onu, C. E., Nwabanne, J. T., Ohale, P. E., Asadu. C. O. (2021). Comparative analysis of RSM,
580 ANN and ANFIS and the mechanistic modeling in eriochrome black-T dye adsorption using
581 modified clay, *South African Journal of Chemical Engineering* 36, 24 – 42.
582 <https://doi.org/10.1016/j.sajce.2020.12.003>
- 583 Onu, C. E., Igbokwe, K. P., Nwabanne, J. T., Charles, O. C., Ohale, P. E. (2020). Evaluation
584 of optimization techniques in predicting optimum moisture content reduction in drying potato
585 slices, *Artificial Intelligence in Agriculture* 4, 39 – 47.
586 <https://doi.org/10.1016/j.aiia.2020.04.001>
- 587 Emembolu, L. N., Ohale, P. E., Onu, C. E., Ohale, N. J. (2022). Comparison of RSM and
588 ANFIS modeling techniques in corrosion inhibition studies of *Aspilia Africana* leaf extract
589 on mild steel and aluminium metal in acidic medium, *Applied Surface Science Advances*,
590 11, 100316. <https://doi.org/10.1016/j.apsadv.2022.100316>
- 591 Jamil, S., Zhonghua, S., Mingshan, J., Zumin, G., Waqas, A. (2018). ANN and RSM based
592 modeling for optimization of cell dry mass of *Bacillus* sp. strain B67 and its antifungal activity
593 against *botrytis cinerea*, *Biotechnol. Biotechnol. Equip.*, 32 (1), pp. 58-68.
594 <https://doi.org/10.1080/13102818.2017.1379359>
- 595 Pakravan, P., Akhbari, A., Moradi, H., Azandaryani, A. H., Mansouri, A. M., Safari, M.,
596 2015. Process modeling and evaluation of petroleum refinery wastewater treatment through
597 response surface methodology and artificial neural network in a photocatalytic reactor using
598 poly ethyleneimine (PEI)/titania (TiO₂) multilayerfilm on quartz tube. *Appl Petrochem Res.*
599 5, 47–59. <https://doi.org/10.1007/s13203-014-0077-7>
- 600 Sodeifian, G., Sajadian, S. A., Ardestani, N. S., 2016. Evaluation of the response surface and
601 hybrid artificial neural network genetic algorithm methodologies to determine extraction yield
602 of *Ferulago angulata* through super critical fluid. *Journal of the Taiwan Institute of Chemical*
603 *Engineers.* 60, 165–173. <https://doi.org/10.1016/j.jtice.2015.11.003>
- 604 Brzezińska-Miecznik, J., Haberko, K., Sitarz, M., Bućko, M. M., Macherzyńska, B. (2015).
605 Hydroxyapatite from animal bones – Extraction and properties, *Ceramics international*,
606 <http://dx.doi.org/10.1016/j.ceramint.2014.12.041>
- 607 Clesceri, L. S., Greenberg, A. E., and Eaton, A. D. Standard Methods for the Examination of
608 Water and Wastewater, American Public Health Association, American Water Works
609 Association, Water Environment Federation, Washington, DC, USA, 29th edition, 1998.
- 610 Coutts, R. T., 2008. In: Chatten, L. G., (ed). *Pharmaceutical Chemistry – Instrumental*
611 *Techniques.* CBS Publishers and Distributors PVT Ltd., New Delhi, India, pp. 59 – 125.
- 612 Ohale, P. E., Nwajiobi, O. J., Onu, C. E., Madiebo, E. M., Ohale, N. J. (2022b). Solvent
613 extraction of oil from three cultivars of Nigerian mango seed kernel: Process modeling, GA -

614 optimization, nonlinear kinetics and comparative characterization, Applied Food Research 2
615 (2), 100227. <https://doi.org/10.1016/j.afres.2022.100227>

616 Nwabanne, J.T., Iheanacho, O.C., Obi, C.C. et al. Linear and nonlinear kinetics analysis and
617 adsorption characteristics of packed bed column for phenol removal using rice husk-activated
618 carbon. Appl Water Sci 12, 91 (2022). <https://doi.org/10.1007/s13201-022-01635-1>

619

620 Onu, C. E., Nweke, C. N., Nwabanne, J. T. (2022c). Modeling of thermo-chemical pretreatment
621 of yam peel substrate for biogas energy production: RSM, ANN, and ANFIS comparative
622 approach, Applied Surface Science Advances, 11, 100299.
623 <https://doi.org/10.1016/j.apsadv.2022.100299>

624

625 Okan, O. L., Ugonabor, V. I., Onu, C. E. and Chinedu J. U. (2022). Application Of Tricking
626 Filter With Hybrid Biofilm Support Media In The Treatment Of Petroleum Effluent, LAUTECH
627 Journal of Engineering and Technology 16 (2), 94-105

628

629 Nwobasi, V. N., Igbokwe, P. K., Onu, C. E. (2022). Optimization of Acid Activated Ngbo Clay
630 Catalysts in Esterification Reaction Using Response Surface Methodology, Asian Journal of
631 Physical and Chemical Sciences, 10(1), 11-27.
632 <https://doi.org/10.9734/AJOPACS/2022/v10i130147>

633

634 Emembolu, L. N., Nwabanne, J. T., Onu, C. E. (2017). Kinetic Modeling of Anaerobic Digestion
635 of Restaurant Waste Water, British Journal of Applied Science & Technology
636 21(4): 1-12. <https://doi.org/10.9734/BJAST/2017/33397>

637

638 Onu, C. E., Nwabanne, J. T. (2014). Application of Response Surface Methodology in Malachite
639 Green Adsorption Using Nteje Clay, Open journal of chemical engineering and science, 1, 2, 19 -
640 33.